ACCURATE RCS IMAGING OF CAR IN-CABIN OBJECTS AT SUB-THZ FREQUENCIES

Victor Pettersson [1], Sining An [2]

[1]Veoneer Research, Veoneer Sweden AB, Vårgårda, Sweden
[2]Department of Microtechnology and Nanoscience, Chalmers University of Technology, Gothenburg, Sweden
**E-mail: [1]victor.pettersson@veoneer.com, [2] sininga@chalmers.se*

Keywords: TERAHERTZ, RADAR CROSS-SECTION, IMAGING, IN CABIN, SENSING

Abstract

Novel efforts to characterize the car-cabin propagation environment at 243 GHz have been made. A Radar Cross-Section (RCS) imaging system is presented for examining the sub-THz scattering properties of individual objects/features found in a typical car cabin. The system is based on Inverse Synthetic Aperture Radar (ISAR) techniques, and aims to accurately estimate the spatial distribution of reflection points off objects from various aspect angles. The resulting data aims to increase the knowledge of the relatively complex propagation environment inside a car cabin, and aid development of in-cabin sensing sub-THz radar systems. Presented are measurements made of a steering wheel and a car seat. Individual reflection points could be resolved by a few centimeters using a 10 GHz bandwidth. The front of the steering wheel, which consisted mainly of smooth plastic, produced rather strong specular reflections whilst the fabric car seat produced less intense but diffuse reflections off its center area.

1 Introduction

In-cabin monitoring is an important enabler in assuring passenger safety of modern cars. Such systems aim to infer passengers' seating position and health status and relay the information to the driver or a central controller. The sub-THz frequency range (100 - 330 GHz) could potentially allow for very compact, non-intrusive in-cabin sensing solutions while at the same time promising high spatial resolution.

In contrast to many other radar use-cases, in-cabin sensing takes place in an enclosed environment made up of various materials with different electromagnetic scattering properties. The propagation conditions become complex, and good knowledge of the scattering properties of in-cabin objects at the frequency band of interest is important to system design. This paper describes in-cabin object characterization efforts made at sub-THz frequencies, specifically 243 GHz, with emphasis on estimating the Radar Cross-Section (RCS) using radar imaging techniques. Here, "characterization" of an object means

- to resolve individual reflection points of an object and measure their intensity at sub-THz frequencies,
- and to identify from what aspect angles the reflection points are visible to the radar.

To the authors' knowledge, no similar measurement campaigns have been documented previously for this specific use-case.

For example, the data gathered from characterization efforts as described here can be used in radar simulations. This very topic is described in [1] for modeling cars and motorbikes at 23 to 27 GHz.

1.1 Radar Cross-Section and Radar Images

In radar systems, the received power is a function of target reflectivity. And the reflective property of an object is usually quantified using the RCS, which is an equivalent area that relates the backscattered power to the incident power density [2]. For a monochromatic signal of frequency f, the returned radar signal from an object is proportional to the integral:

$$S(f) \propto \int_{\mathcal{I}} \rho(\mathbf{r}) e^{-j2\pi f \ell(\mathbf{r})/c} d\mathbf{r} \tag{1}$$

similar to (6.60) in [3]. Here, $\ell(\mathbf{r})$ is the distance traveled by the transmitted radio-frequency waveform, to and from the reflection point at position $\mathbf{r}$, and c is the speed of light in a vacuum. $\rho(\mathbf{r})$ is the spatial square-root RCS distribution, or the "reflectivity distribution", and $\mathcal{I}$ is the illuminated region of the object.

In radar imaging, the aim is to make an image/estimate of $\rho(\mathbf{r})$ in (1) from radar data [3]. In our particular case of Inverse Synthetic Aperture Radar (ISAR), images are formed by coherently processing radar returns off an object which is rotated with regular steps. Rotation can be achieved by placing the object on a rotating table, as illustrated to the left in Fig. 1. This creates a synthetic aperture, or an array of antenna phase centers, around the object which enables high spatial resolution [3]. The angular span over which radar echoes are coherently processed is referred to as the "integration angle".

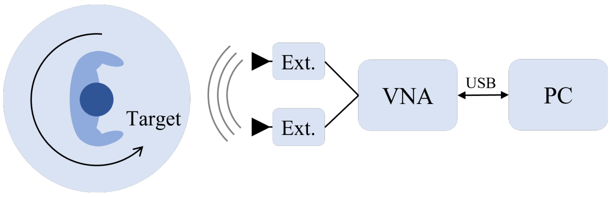

Fig. 1: ISAR measurement geometry and measurement setup.

2 ISAR RCS Imaging

In this work, images are two-dimensional because the measurement setup only applies one axis of target rotation. They should be thought of as a top-down, cross-sectional view of the target reflectivity in a horizontal plane coinciding with the radar.

2.1 Data Model

Assume that a point scatterer, characterized by its spatial position (x_s, y_s) and a constant RCS value σ_s, is located in free space. In our case, the measured return signal from such a target becomes

$$S(f, x_s, y_s) = \alpha(x_s, y_s) e^{-j2\pi f \ell(x_s, y_s)/c} \tag{2}$$

where $\alpha(x_s, y_s)$ is the amplitude response

$$\alpha(x_s, y_s) = \sqrt{\frac{G^2 \lambda_c^2 \sigma_s}{(4\pi)^3 R_{\text{tx}}^2(x_s, y_s) R_{\text{rx}}^2(x_s, y_s)}} \tag{3}$$

and is derived from the square-root of (1.20) in [4]. Here, G is the antenna gain, λ_c is the center wavelength, $R_{\text{tx}}(x_s, y_s)$ is the transmitting antenna-to-target distance and $R_{\text{rx}}(x_s, y_s)$ is the target-to-receiving antenna distance.

For a more realistic scenario, the received radar signal, denoted $S(f)$, is assumed to be a superposition of many components described by (2) from many reflection points at various positions. Such a model can be seen as a discretized, proportional version of (1).

2.2 Image Formation using Backprojection

Radar data is gathered at multiple aspect angles θ spaced by $\Delta\theta$ within an integration angle $\theta_{\text{int.}}$. For each aspect angle, the signal is sampled at frequencies spaced with uniform steps within a certain bandwidth B around a center frequency f_c. One such set of data is referred to as a "frequency sweep" or "sweep". In total, $M = \theta_{\text{int.}}/\Delta\theta$ sweeps are collected and are numbered $m = 0, 1, \ldots, M-1$. The m:th sweep is denoted $S_m(f)$.

To create an image, data is first inverse Fourier transformed

$$s_m(\ell) = \mathcal{F}^{-1}\left\{S_m(f)\right\} \tag{4}$$

and brought into the range domain (or time domain, equivalently). Range domain data is then projected onto a pixel-grid (x, y) by associating each pixel with a two-way distance $\ell_m(x, y)$. At the same time, a spatially variant matched filter is applied along with a scaling factor to produce the pixel-wise estimate

$$\hat{\rho}(x, y) = \\ = \frac{(4\pi)^{3/2}}{G\lambda_c}\left(\frac{1}{M}\sum_{m=0}^{M-1} s_m\left(\ell_m(x, y)\right)\mathcal{C}_m(x, y)\right) \tag{5}$$

where the filter $\mathcal{C}_m(x, y)$ is

$$\mathcal{C}_m(x, y) = R_{\text{tx}}^{(m)}(x, y) R_{\text{rx}}^{(m)}(x, y) e^{j2\pi f_c \ell_m(x,y)/c} \tag{6}$$

and the m-subscript indicates that it varies also with aspect angles. The backprojection and filtering requires good knowledge of the measurement geometry dimensions, as they are needed to calculate $\ell_m(x, y)$, $R_{\text{tx}}^{(m)}(x, y)$ and $R_{\text{rx}}^{(m)}(x, y)$. The filter $\mathcal{C}_m(x, y)$ and image scaling is entirely based on the data model in (2). Evaluating (5) at (x_s, y_s) exactly will give $\hat{\rho}(x_s, y_s) = \langle \sigma_s^{1/2} \rangle$, where $\langle \cdot \rangle$ is used to denote the coherent average, and a corresponding RCS image is produced by taking the magnitude square of (5). The presented algorithm is commonly referred to as the "backprojection algorithm", and a similar variant to what is used here is described in [5].

The backprojection algorithm was initially chosen because it is capable of imaging of near-range targets and accounts for wavefront curvature. This is not the case for many fully Fourier transform-based algorithms [5].

2.2.1 Considering Self-Occlusion and AoI Dependence: A detrimental effect that enter into ISAR images of realistic, non-zero volume targets is "shadowing" or "target self-occlusion", and refers to when the target surface facing the radar occludes reflection points on the opposite side [3]. This effectively limits the per-reflection point integration angle and should be considered when ISAR data is collected over large angles. Also, over large angular spans it is important to consider that the backscattered energy is a function of the transmitted waveform angle of incidence (AoI) upon the target surface, denoted here as ψ. This is especially true when reflections are specular and not diffuse. For a large-angle scan, a single reflection point experiences a wide spectrum of incidence angles throughout the measurement. We rewrite the the reflectivity distribution as $\rho(\mathbf{r}) = \rho(\mathbf{r}, \psi)$ to emphasize this effect.

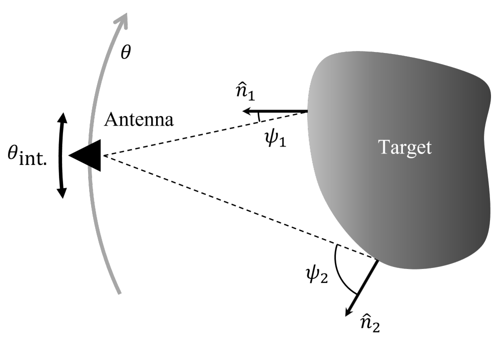

Fig. 2: Illustration of the aspect-angle dependency of the angle of incidence and shadowing.

Both above mentioned effects are also illustrated in Fig. 2 for clarity. In the figure, the AoIs of two arbitrary reflection points, ψ_1 and ψ_2, are clearly functions of the radar aspect angle θ and the object surface normals, denoted $\hat{\mathbf{n}}_1$ and $\hat{\mathbf{n}}_2$.

These effects are important to consider as they will affect the accuracy but also the resolution of produces ISAR images. For example, the image formation algorithm in Section 2.2 implicitly assumes that the expected value of $\rho(\mathbf{r}, \psi)$ remains constant during the coherent averaging throughout the integration angle. Therefore, any fluctuations due to a change in AoI or self-occlusion will create a bias and decrease accuracy. Image resolution is discussed later in Section 2.3.

2.2.2 Section Images and the Summary Image: In order to combat the problems highlighted in Section 2.2.1, image data collected over large angles are divided up into much smaller, overlapping angular sections. Each section is processed coherently according to the procedure described in Section 2.2 and then combined. This procedure aims to produce more accurate images based on the fact that, for smaller spans of θ, we can approximate the AoI ψ for an arbitrary reflection point located at $\mathbf{r}$ as being constant. This allows for approximating $\rho(\mathbf{r}, \psi) \approx \rho(\mathbf{r})$ during the coherent averaging interval, and should produce an unbiased estimate in theory. With a similar argument, the procedure also avoids target self-occlusion effects.

The images corresponding to each angular section, referred to as "section images", can be combined using a $\max$-operation across the magnitude of all images. The resulting image is a summary of the most significant recorded reflectivity values throughout the large angle measurement, and is therefore referred to as the "summary image". If the section images are numbered $q = 0, 1, \ldots, Q-1$ where $\hat{\rho}_q(x, y)$ is the q:th section image formed according to (5), then the reflectivity summary image becomes

$$I(x, y) = \max_q |\hat{\rho}_q(x, y)|. \tag{7}$$

Assume that each section overlaps the previous by $\alpha \times 100\,\%$, then the center aspect angle $\theta_c(q)$ corresponding to the q:th section becomes

$$\theta_c(q) = \theta_{\text{int.}}/2 + q(1-\alpha)\theta_{\text{int.}} \tag{8}$$

where $(1-\alpha)\theta_{\text{int.}}$ is the aspect-angle step between sections. This means that we can associate each section image with a certain aspect angle. As a result, by inspecting individual section images or sequences of section images it is possible to see the aspect-angle dependency of individual reflection points. This will in turn also yield information regarding their AoI dependence, and conclusions regarding the nature of the reflection (i.e. specular or diffuse) can be made.

2.3 Image Resolution and Sampling Criterion

Typically the range resolution is

$$\delta_R = \frac{c}{2B} \tag{9}$$

in radar systems, and this is also true for the system used in this work. According to (7.1) in [6], the cross-range resolution in ISAR/SAR is:

$$\delta_{\perp R} = R\frac{\lambda_c}{2L_{\text{ISAR}}} = R\frac{\lambda_c}{2r\theta_{\text{int.}}} \tag{10}$$

where R is the radar-to-target range and L_{ISAR} is the synthesized aperture length. The right-most expression is modified for the ISAR geometry, where $L_{\text{ISAR}} = r\theta_{\text{int.}}$ and r is the distance from the radar to the rotating table center.

In order to produce a useful image, aliasing must be avoided. By making sure that the angle spacing in between sweeps satisfies

$$\Delta\theta \leq \frac{\lambda_c}{2D_{\text{min}}} \tag{11}$$

the radar signal phase will be sampled correctly [7]. The parameter D_{min} is the diameter of the smallest sphere, centered at the table center of rotation, that can contain the target-to-be-imaged entirely.

3 Simulated Results

A simulation was set up in MATLAB in order to investigate the effects of AoI and target self-occlusion in ISAR images and to verify the accuracy of the proposed summary image from Section 2.2.2 for large collection angles. Two point scatterers were simulated, one with $10\,\text{m}^2$ RCS and another with $1\,\text{m}^2$ RCS. The scatterers were located at coordinates (14,12) cm and (12,12) cm, respectively, and the radar was positioned $200\,\text{cm}$ from the simulated rotating table center placed at (0,0) cm. The point scatterers where then rotated $360°$ at a constant speed and the radar returns were calculated according to the data model in (2) at regular time intervals. The angular step was chosen considering (11) for the outer-most scatterer which is located approximately $18\,\text{cm}$ from the table center, meaning that $D_{\text{min}} = 36\,\text{cm}$ and $\Delta\theta \leq 0.1°$. The signal center frequency was set to $f_c = 243\,\text{GHz}$, and a bandwidth of $B = 10\,\text{GHz}$ was used. In the end, complex white Gaussian noise was added to the signal resulting in a simulated $40\,\text{dB}$ signal-to-noise ratio.

A simple rectangular window is applied to the point targets' reflectivity to simulate AoI and self-occlusion effects. This is illustrated in Fig. 3, where the targets are represented by black dots. The point targets are only visible to the radar when they pass through the $15°$ wide shaded area directly in front of the antenna, meaning they have non-zero RCS only there.

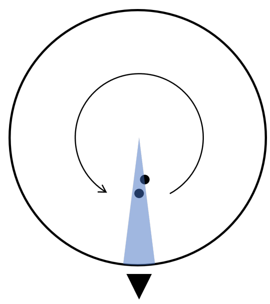

Fig. 3: Simulated ISAR scenario.

Two resulting images are shown in Fig. 4a and 4b. The former image applies a $360°$ integration angle whilst the latter is a summary image of sections with $\theta_{\text{int.}} = 10°$. In both cases the range resolution amounts to $1.5\,\text{cm}$ by measuring the peak-to-first-null width of the mainlobes of the strongest target in the range dimension, which is directed radially from $(0, 0)$ in the images. This is consistent with (9): $\delta_R = c/(2B) = 1.5\,\text{cm}$.

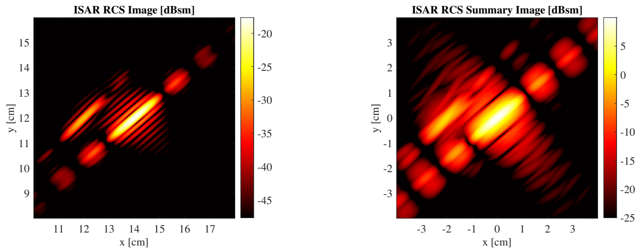

(a) (b)

Fig. 4: (a) ISAR image using $360°$ integration angle, (b) ISAR RCS summary image.

The image in Fig. 4a achieves a finer cross-range resolution than the image in 4b. This is reasonable because it processes the radar return signal coherently over an effective $15°$ angular span, and the integration angle applied in Fig. 4b is $10°$. The cross-range dimension is perpendicular to the range dimension in the images. According to theory, the cross-range resolution of the image in 4b should amount to approximately $3\,\text{mm}$ for the stronger target using (10) with $R = 2.00 - 0.18\text{m} = 1.82\,\text{m}$. However, measured from the image, the cross-range resolution is closer to $6\,\text{mm}$. This is due to the max operation performed on consecutive section images, resulting in blurring of the mainlobe but also the sidelobes as can be seen in the image.

With regards to the accuracy, the strongest peak in Fig. 4a measures $-17.7\,\text{dBsm}$ (decibel square meters) and is clearly biased - the true value is $10\,\text{dBsm}$ or $10\,\text{m}^2$. The corresponding peak in the summary image measures $9.97\,\text{dBsm}$ and is more accurate. The weaker target with a true RCS of $0\,\text{dBsm}$ or $1\,\text{m}^2$ is registered at $-0.39\,\text{dBsm}$.

4 Data Acquisition

The experimental ISAR measurement geometry is shown in Fig. 1. The image shows a bistatic radar arrangement, realized by two horn antennas connected via two frequency extender modules to a vector network analyzer (VNA). The two antennas were separated by $8.3\,\text{cm}$ using a custom antenna fixture. Both the transmitting and receiving polarization were horizontal (HH). As mentioned, the radar observed a target placed on a rotating table which was rotating at a constant speed, and the speed was chosen depending on the size of the target-to-be-imaged according to (11). The target was centered with the table center of rotation, which was approximately $2.0\,\text{m}$ from the radar. Measurements were conducted in a rather small lab environment, and some clearance around the rotating table was maintained in order to avoid multibounce conditions. Sweeps were collected at 401 linearly increasing, uniformly spaced frequency points within a $B = 10\,\text{GHz}$ bandwidth centered at a frequency of $f_c = 243\,\text{GHz}$. The time in between each sweep was $100\,\text{ms}$, and the timing coordination was handled by VNA-control software on a PC connected via USB.

4.1 Hardware

The VNA used was a Keysight N5242A PNA-X Microwave Network Analyzer with a frequency range of 26.5 GHz. The extenders were VDI model WR3.4-VNAX, which operate at frequencies ranging from 220 to 330 GHz. The antennas are ERAVANT WR-03 pyramidal horn antennas with a 220 to 325 GHz operating range and a defined nominal gain of 25 dBi, which corresponds to a 10 degree 3 dB beamwidth in both the E- and H-planes. An S11-parameter measurement may theoretically identify the reflected signal using a single-port measurement with one extender module (monostatic radar). However, due to the significant path loss of the H-band signal, an internal reflection was observed with this setup, and it was far stronger than any exterior reflection. As a result, two extender modules were employed in place of the original to perform S21-parameter measurements.

4.1.1 Amplitude Calibration: The VNA was first calibrated at the reference plane of the extender wave guide flanges, but the signal amplitude must still be calibrated against uncertainties in the radar antenna gain. The gain was assumed constant over the scope of the rotating table, which is reasonable if the radar is placed far away enough. In this work, the antenna gain was calibrated using a metallic sphere of known RCS. The calibrated antenna gain is

$$G = G_{\text{uncal.}} \left(\frac{\sigma_{\text{app.}}}{\sigma_{\text{sphere}}} \right)^{1/2} \tag{12}$$

where $G_{\text{uncal.}}$ is the uncalibrated gain, σ_{app} is the apparent RCS of the sphere reference target, measured with the radar, and σ_{sphere} is the theoretical, known RCS of the sphere. A similar procedure is described in [4].

5 Measurements & Imaging Results

This paper presents the imaging result of two different car in-cabin objects: a steering wheel and a car seat. Because of their different size, two different values of angular spacing $\Delta\theta$ was used: $0.08°$ and $0.05°$, respectively. Both are scanned for a total of $180°$ (front sides), resulting in collection times of approximately four and six minutes.

The RCS section and summary images presented here apply a $\theta_{\text{int.}} = 5°$ integration angle, where each section is overlaps the previous by $25\,\%$ such that two consecutive sections correspond to a $(1 - 0.25) \times 5° = 3.75°$ step in aspect angle.

In order to reduce the intensity of the sidelobes, which caused the image in Fig. 4b to look "messy", a Hamming window was applied to the data in both dimensions. Windowing causes a slight bias, so images were calibrated against other versions of the same image produced without any window function applied. The resulting RCS summary images are shown in Fig. 5b and Fig. 6b of the steering wheel and car seat, respectively, along with reference pictures in Fig. 5a and Fig. 6a. As mentioned, the images are to be interpreted as a top-down view of the objects in the same horizontal plane as the radar. In the case of the car seat, the radar was aligned vertically with the back rest, and this is what is seen in Fig. 6b. Both objects are facing to the left in the images, and we can think of the radar as scanning the objects moving clockwise from the negative y-axis, passing the negative x-axis, and stopping close to the positive y-axis. Thus, we reference the aspect angles from the negative y-axis, and the radar faces the front of the objects after 90° of rotation.

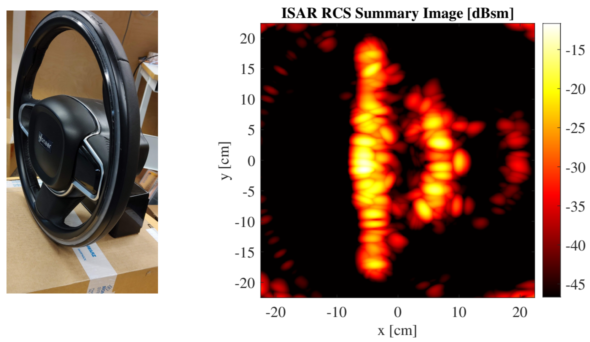

(a) (b)

Fig. 5: (a) Picture of steering wheel, (b) ISAR RCS summary image of steering wheel.

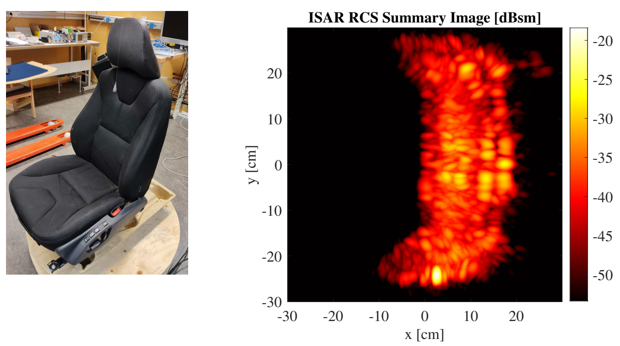

(a) (b)

Fig. 6: (a) Picture of car seat, (b) ISAR RCS summary image of car seat.

From the two images in Fig. 5b and 6b, we can make out that the steering wheel produces its strongest reflections of about -15 to $-10\,\mathrm{dBsm}$ off the plastic front cover. The car seat is covered with fabric, and evidently produces less intense reflections. Most reflection points visible in Fig. 6b registers values of around -35 to $-30\,\mathrm{dBsm}$. The resolution cells seem to have a largest dimension of approximately $1.5\,\mathrm{cm}$, which corresponds to the range resolution. They are thus more limited by the system bandwidth rather than the chosen integration angle in this particular case.

As mentioned in the last paragraph of Section 2.2.2, individual section images or sequences of section images can be analyzed in order to see the aspect-angle or AoI dependency on a reflection point-to-reflection point basis. In Fig. 7, two section images are displayed side-to-side from the steering-wheel data.

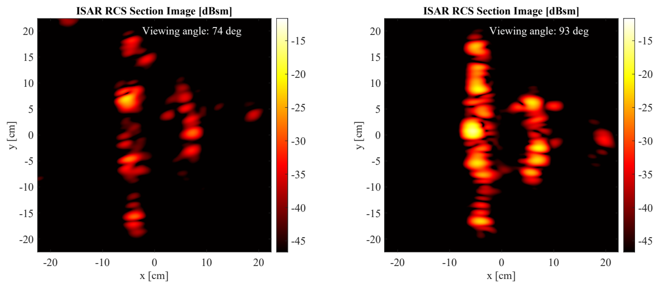

Fig. 7: Section images of the steering wheel.

The left section is from an aspect angle of 74°, such that the angle of incidence onto the steering wheel front cover is, by a rough estimate, 15° to 20° based on the image orientation. Visible reflection points are off the steering wheel outer ring and from protruding details of the front cover. Then, after an approximately 19° rotation the radar faces the front cover head-on. Now it produces a strong reflection seen in the right image section of Fig. 7. The strong angle-of-incidence dependence indicates that the rather smooth plastic surface of the front cover produces specular reflections, rather than diffuse. This result also verifies the effects discussed in Section 2.2.1, and illustrates the need for accurate, section-wise analysis for large-angle ISAR imaging.

Also, the right image section of Fig. 7 shows significant reflections behind the steering wheel front cover. These reflections are most likely due to metal parts of the steering wheel mount, and can evidently be detected through the plastic cover.

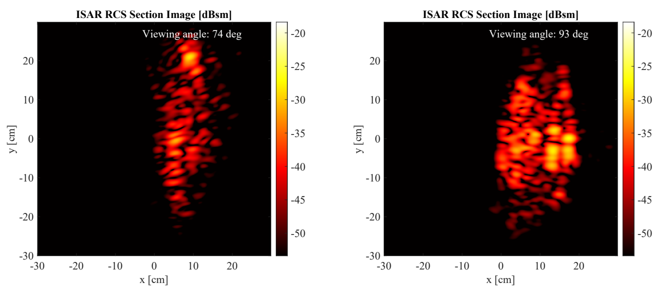

Fig. 8: Section images of the car seat.

Lastly, two section images of the car seat, at similar aspect angles as in Fig. 7, are displayed in Fig. 8. Reflections of the center part of the car seat back rest are visible in both section images, indicating that the surface of the fabric produces diffuse reflections. Notably, only parts of the back rest are illuminated at each image section in Fig. 8. This likely due to the narrow 10° half-power beamwidth of the antennas, as they might not illuminate the whole back rest at one time.

6 Discussion

From the steering wheel and car seat results, it is evident that ISAR RCS imaging can act as an intuitive tool for locating major reflection points off various objects. Large angular scans provide additional information with section images, providing information about "when" a certain reflection point is visible which in turn makes it possible to draw conclusions regarding the object material characteristics.

Traditionally, the RCS is measured for targets/objects contained entirely in the resolution of the radar system. Here, the system resolution is much finer than the objects themselves, and it is believed that this causes the RCS image values to become dependent on the size of the resolution cell. The authors identify this as a general problem in high-resolution, near-range imaging scenarios, and it is important to note that the relation between the resulting RCS values gathered in this paper and the received power in a potential operating sub-THz in-cabin radar system is not straight forward. This is unless their resolution is the same. Thus, the mean value of the entire image is perhaps less meaningful compared to the spatial information and relative amplitudes.

7 Conclusion

Sub-THz, near-range ISAR imaging efforts at 243 GHz have been conducted in an enclosed lab environment and have resulted in useful results. Measurements of two different objects typically found in a car cabin and of different materials have been made. Using ISAR images, it is possible to locate major reflection points off objects and resolve them on a centi-meter level using a 10 GHz bandwidth. For large collection angles, the nature of each reflection point can be analyzed with regards to its aspect-angle and AoI dependence. This in turn gives information about the electromagnetic scattering properties of various materials and geometries. Evidently, the flat plastic cover of the measured steering wheel gives off strong specular reflections whilst the fabric car seat produces comparably less intense and diffuse reflections.

It was postulated that self-occlusion and AoI effects are present when measuring real objects, and this was verified and also mitigated using section-wise imaging. For large collection angles, the summary image was shown in simulations to be more accurate in regards to the reflection point intensities but can sometimes result in coarser cross-range resolution.

8 Acknowledgements

This project has received funding from the European Union's Horizon 2020 research and innovation programme under grant agreement No. 824962. We would like to thank the Car2TERA project consortium members and reviewers for encouraging words and valuable input. We are thankful for the many technical discussions with Olof Eriksson, Hans Herbertsson and Zhongxia Simon He. Thank you to Viet Lê for introducing us to his measurements, and showing us how to control the VNA with Python. At last, a big thank you to our colleagues John, Johan and Daniel of the Veoneer Concepts and Validation-team for putting together the rotating table and producing the antenna fixture.

9 References

[1] T. Schipper, J. Fortuny-Guasch, D. Tarchi, L. Reichardt, and T. Zwick, "Rcs measurement results for automotive related objects at 23-27 ghz," in *Proceedings of the 5th European Conference on Antennas and Propagation (EUCAP)*, 2011, pp. 683–686.

[2] R. J. Sullivan, *Radar Foundations for Imaging and Advanced Concepts*. Raleigh NC: SciTech Publishing Inc., 2004, ch. 3.

[3] ——, *Radar Foundations for Imaging and Advanced Concepts*. Raleigh NC: SciTech Publishing Inc., 2004, ch. 6.

[4] ——, *Radar Foundations for Imaging and Advanced Concepts*. Raleigh NC: SciTech Publishing Inc., 2004, ch. 1.

[5] Y. Ding and D. Munson, "A fast back-projection algorithm for bistatic sar imaging," in *Proceedings. International Conference on Image Processing*, vol. 2, 2002, pp. II–II.

[6] R. J. Sullivan, *Radar Foundations for Imaging and Advanced Concepts*. Raleigh NC: SciTech Publishing Inc., 2004, ch. 7.1.

[7] D. Mensa, S. Halevy, and G. Wade, "Coherent doppler tomography for microwave imaging," *Proceedings of the IEEE*, vol. 71, no. 2, pp. 254–261, 1983.